Waves in Random Media 6 (1996) 361–386. Printed in the UK

Ultrasonic investigation of the vibrational modes of a sintered glass-bead percolation system

H P Schriemer, N G Pachet and J H Page

Department of Physics, University of Manitoba, Winnipeg, MB, Canada R3T 2N2

Received 1 February 1996

Abstract. A physical realization of a random structural percolation system, formed from sintered glass microspheres, has allowed its elasticity and vibrational dynamics to be studied using ultrasonic techniques in the 1–55 MHz frequency range. Samples with occupied volume fractions ϕ between 0.18 and 0.64 were prepared, enabling the percolation threshold $\phi_c = 0.19 \pm 0.01$ to be determined. From measurements of the ultrasonic velocity, the elasticity exponent τ was found to be 2.9 ± 0.1, which falls midway between the best theoretical estimates for scalar and bond-bending elasticity. Very low values of Poisson's ratio were observed, and data for the longitudinal and shear wave velocities were shown to be consistent with the Arbabi–Sahimi suggestion that the ratio of the bulk to shear moduli approaches the value $8/z$ near threshold, where z is the coordination number. The frequency dependence of the scattering mean free path, l_s, was measured over an extended range of wave vectors k, corresponding to $1.6 < kl_s < 60$, and spanning the transition from weak to very strong scattering. The mean free path was found to scale with a characteristic length, l_c, proportional to the percolation correlation length below which the structure exhibits fractal correlations. Comparison of the scaling behaviour for longitudinal and shear waves suggests that there may be a unique frequency for both polarizations, rather than a length scale, that characterizes the breakdown of the coherent propagation of acoustic waves due to very strong scattering.

1. Introduction

Over the past decade, there has been considerable interest in using percolation theory to model the static elasticity and vibrational dynamics of random systems. This is because of the relatively simple structure of a percolating network, which makes theoretical prediction and numerical simulation of the physical behaviour feasible. The static elasticity of random percolating structures is of particular interest since the various different microscopic elasticity models predict vastly different critical exponents. Percolation systems, which consist of sites randomly occupied with probability p, are known to exhibit fractal geometry at short length scales and Euclidean geometry at long length scales; the transition between these two regions occurs at the percolation correlation length ξ. The critical probability, or percolation threshold p_c, is the value of p above which an infinite cluster of connected sites (or bonds) exists. The vibrational dynamics of these random systems for $p > p_c$ is expected to be quite intriguing, since a crossover is predicted in the vibrational spectrum from extended phonon excitations to fracton excitations; these fractons are predicted to be localized if the fracton dimension $\tilde{d}$ is less than two. A percolation system, being fractal at short length scales and homogeneous at long length scales, is thus well suited for modelling random systems which manifest similar behaviour.

0959-7171/96/040361+26$19.50

The first experimental system in which these predictions were tested consisted of sintered metal powders. Deptuck *et al* performed measurements on beams of sintered, submicron, silver powder and found that the elasticity critical exponent was significantly greater than the conductivity critical exponent [1], implying that elasticity belongs to a different universality class to conductivity. Moreover, the observed value of the elasticity exponent agreed well with that predicted by a vector model of the elasticity of percolating networks [2]; this vector model, unlike the simple scalar model which maps onto the same equations of motion as the conductivity, incorporates local bending of the backbone of the infinite cluster and thus predicts a more rapid decrease in the rigidity of the structure as the percolation threshold is approached. This elasticity behaviour was also confirmed by Maliepaard *et al* in ultrasonic measurements on the same system [3]. In addition, by performing experiments over a range of ultrasonic frequencies, they found that a band edge exists beyond which sound does not propagate. Further ultrasonic experiments on copper powder sinters by Page and McCulloch [4] confirmed this behaviour, supporting theoretical predictions of a crossover from extended phonon excitations to localized fracton excitations.

Silica aerogels form a different class of porous materials which have been extensively studied using a range of different experimental techniques. These experiments have been extremely successful in investigating the predictions of the dynamical properties of fractal structures, despite the fact that they do not map directly onto a percolating network. However, it has been indicated that if the structure is unequivocally fractal, the experimental data may be adequately described by scaling theory, although quantitative agreement with the predicted critical exponents is not expected [5]. Using small-angle neutron scattering (SANS), aerogels have been found to exhibit fractal structure over at least an order of magnitude in length, depending on the porosity [6]. A phonon–fracton crossover was first observed in aerogels using Brillouin spectroscopy [7, 8] and the behaviour of fractons has since been investigated using a range of other techniques, such as inelastic neutron scattering and Raman scattering; see Nakayama *et al* for an excellent review of the theoretical, as well as experimental, literature [5]. The density of states is determined by these techniques, giving a direct measure of the fracton dimension $\tilde{d}$; this can be simply related to the elasticity exponent mentioned above. The fracton dimension in aerogels was found to take on different values depending on the frequency range investigated and the preparation conditions of the aerogel. At low frequencies near the phonon–fracton crossover the fracton dynamics is expected to be dominated by bond-bending elastic interactions. Thus, it was a considerable surprise that the observed values of $\tilde{d}$ were found to be much larger than predicted for the bond-bending models, being extremely close to the scalar elasticity value $\tilde{d} = 4/3$. This discrepancy initially led to considerable confusion about the nature of the microscopic elasticity in aerogels. This confusion has now been resolved with the realization that a high degree of internal connectivity in aerogels can cause the bond-bending fracton dimension to be much higher than the value predicted for percolation models [9, 10].

The motivation of our present work is to investigate experimentally the static elasticity and vibrational dynamics of a porous random solid that is more directly described by a simple structural percolation model. To this end, we have performed ultrasonic experiments on glass-bead sinters constructed so as to form nearly ideal examples of percolating networks [11, 12]. This was accomplished by mixing glass beads with a second powder of similar grain size, which was removed after sintering the glass. Thus, the positions of the glass particles and voids were controlled in a way that corresponds to percolation models. To probe the elasticity of the glass-bead sinters, we measured the ultrasonic velocity of the ballistic pulse that propagates without scattering through the medium, and obtained new information on the exponent τ that describes the weakening of the elasticity as the occupied

volume fraction of glass is lowered. Interestingly, we find that this exponent is not in agreement with either the scalar or the bond-bending models of the elasticity of a percolating system, being approximately midway between the two. To probe the dramatic increase in scattering that occurs as the frequency is increased, we measured the ultrasonic attenuation of the ballistic pulse, allowing the scattering mean free path, l_s, to be determined in a region where ballistic propagation begins to break down. Comparison of the scattering mean free paths for longitudinal and shear wave propagation indicates the unexpected result that this breakdown in coherent propagation occurs at a common frequency for both polarizations, rather than at a common wavelength or length scale. This question has not been addressed in previous theoretical and experimental investigations, which have focused on longitudinal modes.

2. Theory

In this section, we summarize the recent theoretical ideas that have been developed using percolation theory to describe the static elasticity and vibrational dynamics of random disordered systems [5]. If we have an infinite array of lattice sites occupied with a probability p, then there exists a critical probability p_c (the percolation threshold) above which there is an infinite cluster of connected sites and below which there is not. We are interested exclusively in the behaviour of the infinite cluster for $p \geqslant p_c$. As p_c is approached from above, the correlation length ξ, corresponding to an average radius of the largest holes in the cluster [13], diverges. The critical exponent ν is defined such that $\xi \propto (p - p_c)^{-\nu}$, where numerical calculations have determined that, for three dimensions, $\nu = 0.88$ [14]. For experimental systems such as ours, it is the occupied volume fraction ϕ that is the experimentally controlled variable. If we assume that random percolation belongs to the same universality class as lattice-based percolation, then we would expect

$$\xi \propto (\phi - \phi_c)^{-\nu} \tag{1}$$

with the same value of ν.

At long length scales ($R \gg \xi$), the vibrational modes of a porous solid are sound waves (i.e. phonons). The relation between the frequency ω and the wave vector k is then given by the phonon dispersion relation, which, in the Debye model, is $\omega = vk$, where v is the speed of sound. For short length scales ($R \ll \xi$), however, the structure is fractal, and the corresponding excitations are referred to as fractons [15]; the fracton dispersion relation is expected to be different, and is given by $\omega = bk^a$ [16], where a and b are constants. It is expected that the vibrational modes should show a crossover from phonons to fractons when the phonon wavelength is comparable with the correlation length. More precisely, this crossover is expected to occur at a wave vector k such that $k\xi = 1$ [17]. The assumption that the phonon and fracton dispersion relations join continuously at this crossover implies $v \propto \xi^{(1-D/\tilde{d})}$, where D is the fractal dimension, and $\tilde{d} = D/a$ is the fracton dimension that characterizes the vibrational density of states in the fractal regime, $g(\omega) \propto \omega^{(\tilde{d}-1)}$. Thus, the low-frequency phonon velocity should scale as

$$v \propto (\phi - \phi_c)^{y} \tag{2}$$

where $y = \nu(D/\tilde{d} - 1)$.

The scaling behaviour of the phonon velocity can also be expressed in terms of the critical exponent τ that describes the rate at which the macroscopic elastic moduli C shrink to zero as the percolation threshold is approached from above. This critical exponent is defined by the relation $C \propto (p - p_c)^{\tau}$, and is expected to have the same value for any of

the elastic moduli (e.g. bulk, shear or Young's) near p_c. Since elastic moduli are given by the product of density and velocity squared, this implies that

$$v \propto (\phi - \phi_c)^{(\tau-\beta)/2} \tag{3}$$

where β is the density exponent, defined by $\rho \propto (\phi - \phi_c)^{\beta}$ and found numerically to have the value $\beta = 0.44$ in three dimensions ($d = 3$) [18]. Comparison of (2) and (3) leads to the following relationship between the fracton dimension $\tilde{d}$ and the critical exponent τ:

$$\tilde{d} = \frac{2(d\nu - \beta)}{\tau - \beta + 2\nu} \tag{4}$$

thus allowing the fracton dimension to be readily calculated from theoretical estimates of the elasticity exponent [19].

Over the past decade, there has been extensive theoretical interest in the elasticity of random percolating structures, where the main focus has been to show how different microscopic models of the elastic forces between the primary particles lead to distinct universality classes with different values of the critical exponent τ. The first, and simplest, model to be considered was the scalar Born model [20], for which the equations of motion for the elasticity have the same form as those for the conductivity, with the result that the elasticity and conductivity critical exponents, τ and t, are equal. In three dimensions, this gives $\tau = t = 2.0$ [21], so that $\tilde{d} = 1.33$ in agreement with the conjecture of Alexander and Orbach that $\tilde{d} = 4/3$ [15]. While this model has been extensively used in calculations of the dynamics of fractal lattices [5], it ignores the tensorial nature of elastic forces which is expected to play an important role in experimental percolation systems. Probably the most realistic vector percolation model is the bond-bending model, first applied to percolation networks by Kantor and Webman [2]. Here, the elastic energy consists of a central force component acting along the axis of intact bonds plus a bond-bending component arising from the change in angle between bonds. Near p_c, Kantor and Webman showed that the weak bond-bending forces of the singly-connected chains dominate the elasticity of the percolation network, and obtained a lower bound for the critical exponent $\tau = d\nu + 1 = 3.64$ in three dimensions. Subsequent calculations and simulations [14, 22–28] have confirmed that τ is indeed much larger than t for this vector percolation model, and have established more precise estimates of τ. In three dimensions, recent numerical calculations for both bond and site percolation give $\tau = 3.75 \pm 0.11$ [21], consistent with the earlier suggestion that $\tau = t + 2\nu$ [25, 26]. Substituting this value of τ in (4) gives a much lower value for the fracton dimension than was obtained for scalar elasticity, $\tilde{d} = 0.87$, which is very close to the original estimate for bond-bending elasticity, $\tilde{d} = 0.89$, obtained by Webman and Grest [19].

The attenuation coefficient $\alpha(\omega)$ of an ultrasonic wave propagating through an attenuating medium of thickness x is defined by

$$I(x) = I_0 e^{-\alpha(\omega)x} \tag{5}$$

where I is the wave intensity at position x and I_0 is the incident intensity. If the inelastic component of the attenuation is negligible relative to the elastic component (i.e. if scattering dominates over absorption), the attenuation coefficient for ballistic propagation through the medium is given by the inverse of the elastic scattering mean free path, $l_s(\omega)$. At low frequencies, the vibrational wavelengths are much larger than the inhomogeneities in the medium and the scattering is weak; thus, the attenuation is low and the vibrational modes are correctly described by extended acoustic waves. As the frequency is increased, a condition is eventually attained for which the wavelength of the vibration is of the same size as the inhomogeneities. If the scattering is sufficiently strong, the familiar propagating wave

description breaks down and the phonons may become localized. The presence of very strongly scattered sound and the corresponding very short values of the scattering mean free path are prerequisites to localization. By analogy with related problems in electronic systems, the criterion for localization is usually taken as the Ioffe–Regel condition [29] that the elastic mean free path be sufficiently short that $kl_s \leqslant 1$.

Since the ballistic attenuation at fixed frequency depends directly upon the size of the scatterers, the same scattering behaviour should be seen when both the scatterers (i.e. the pores) and the wavelength of the probing frequency are changed proportionally. This is the physical basis of single-parameter scaling theory arguments, which here predict that the attenuation in the phonon regime should scale with the percolation correlation length ξ. Thus the attenuation of any percolating sample due to elastic scattering will have the same wavelength dependence, and will fall on a common curve when attenuation and wavelength are both scaled by ξ. This gives a simple prediction for ultrasonic attenuation in percolation systems that can be directly investigated experimentally.

3. Experiment

In a percolating structure sites are occupied with probability p or unoccupied with probability $1-p$. Thus, to construct an experimental realization of a percolation network, it is necessary to have some means whereby the occupancy of the sites can be controlled in an analogous manner. This was achieved by mixing glass microspheres with nickel powder of similar grain size. The nickel powder, whose sole function was to determine the position of sites unoccupied by the glass beads, was removed by etching after the glass beads were sintered. By varying the amount of nickel, the occupied volume fraction of glass could be made as low as desired. Two sample sets, A and B, were prepared.

The samples from set A were formed using glass spheres of radius 1.1 ± 0.3 μm mixed with nickel powder of radius 1.4 ± 0.3 μm. The mixture was then carefully packed in a die so as to minimize the density variations. It was then pressed, forming a pellet about 13 mm in diameter and of the order of 1 mm thick. The pellet was then removed from the die and sintered at 648° C in air, for 62 ± 2 minutes to form bonds between the glass beads. It was then polished to a flat parallel disc and the nickel particles removed by etching in nitric acid.

The samples from set B were formed using glass beads of radius 0.8 ± 0.2 μm. The glass beads were again mixed with nickel powder, ground together, and pressed into a pellet. To improve the sample homogeneity, this procedure was repeated many times, thus smoothing the irregular nickel surfaces and leading to a more uniform packing [30]. The mixture was then placed in a die and a few drops of methanol were added to assist in the elimination of voids caused by non-uniform settling of the powder. The macroscopic homogeneity was further improved by allowing the mixture to settle in an ultrasonic bath while still wetted with methanol. The sample was then pressed, and sintered in the die at 615° C for 60 ± 2 minutes in a nitrogen atmosphere. The pellet was then polished and etched. Figure 1 shows an example of a sintered sample after etching.

The choice of sintering times and temperatures was dictated by the requirement that the sintering be easily reproducible and that the bonds between the glass beads be neither too strong nor too weak. In figure 1, the neck radius between sintered beads is about one half the mean bead radius and is roughly independent of the actual bead size (within our range of bead sizes); this is because small beads sinter faster than larger ones and form proportionally larger necks. This degree of sintering was chosen as optimal since it produced a relatively robust sample while still maintaining evidence of the sphericity of the constituent glass

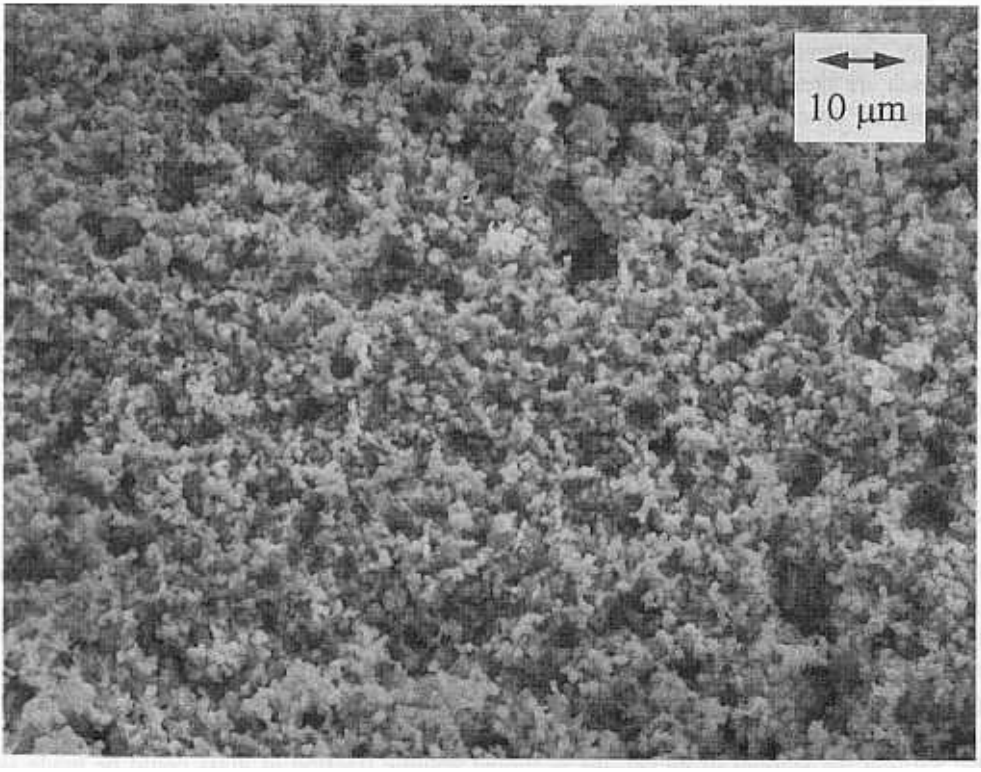

Figure 1. One of the sintered glass-bead samples from set B, prepared as described in the text.

particles. Since the thermal expansion coefficient of nickel is greater than that of glass, no internal strain or microstructure damage due to differential thermal contraction was caused for sample set B as the samples were cooled from the sintering temperature to room temperature. In set A, however, the samples were sintered in air and this caused the nickel particles to become oxidized during sintering, thereby increasing their size. As a result, the bonds between the glass beads, having been weakened by the expansion of the oxidizing nickel particles, were much less robust than those of set B where no oxidation occurred. These two different sample preparation techniques allowed the effects of internal strains on the bulk properties of the sample to be investigated.

The vibrational modes of this structural percolation system were studied by propagating ultrasonic waves through the glass-bead samples. Each sample was placed between two piezoelectric transducers, and a voltage pulse $\sim 2\ \mu s$ long, in the frequency range 1–55 MHz, was used to excite one of the transducers, producing an acoustic pulse. At the sample interface, the pulse was partially reflected and partially transmitted. The transmitted pulse was detected by the receiving transducer on the opposite side of the sample. The attenuation in the sample was normally sufficiently large that multiple reflections of ultrasound in the sample were negligibly small. A block diagram of the experimental setup is shown in figure 2. The attenuator placed on the output of the pulse generator was used to limit the power output from the pulsed radio frequency (RF) voltage source so as not to overdrive the transducer and distort the generated waveform. The other attenuators were used to take precision amplitude measurements which were independent of any nonlinearity in the receiving amplifier. The digital delay generator allowed precision measurements of the

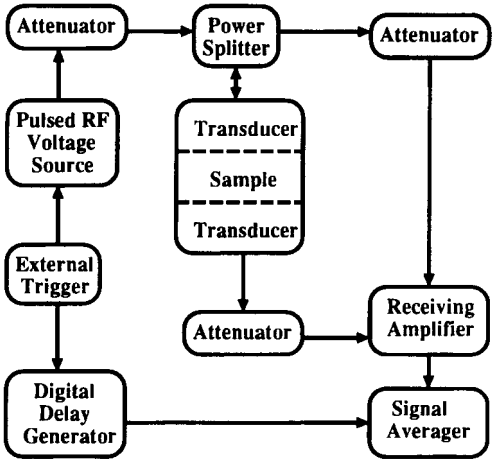

Figure 2. Block diagram of the ultrasonic equipment.

sample transit time (and hence velocity) to be taken.

Both longitudinal and shear mode transducers were used in these experiments. Two different types of longitudinal transducer were used, one made from PVDF (a piezoelectric polymer) and the other from PZT (lead zirconium titanate). PZT-4 transducers were used for the shear measurements. The transducers were bonded with epoxy to fused quartz delay rods which were inserted between the transducers and the sample. The purpose of these delay rods was to introduce a time delay between the initial pulse and subsequent reflections at the interfaces, thus allowing the sensitive receiving amplifier to recover from saturation by the initial high-power pulse from the RF generator. Bonding the transducers to the delay rods also improves the impulse response of the PZT transducers since the acoustic impedance of the transducers is much better matched to the delay rods than to the samples; this allows the acoustic energy to be very efficiently coupled out of the transducer, thereby reducing transducer ringing. The use of delay rods also enables the ultrasonic transit time through the sample to be conveniently measured from the time delay between the reflected pulse (which travels from the generating transducer up and down the first delay rod only) and the transmitted pulse (which passes once through the sample and each delay rod).

The samples were then bonded to these delay rods using very thin layers of Nonaq stopcock grease. To ensure that the Nonaq bonding layer was extremely thin and uniform, a small amount was applied to one of the delay rods and the two delay rods were wrung together to spread the Nonaq evenly. It has been estimated that good bonds less than 1 μm thick were routinely achieved. Nonaq was used because it is sufficiently viscous that there was negligible penetration of the grease into the porous sinter. A holder, shown in figure 3, was designed to support these delay rods so that their separation and parallelism could be precisely controlled by adjusting the three micrometer support posts. This was essential for the fragile samples studied in these experiments, to avoid both crushing the samples while performing the measurements and spurious reduction in the detected signals from the transducers owing to phase cancellation associated with non-parallelism. The micrometers could be set to a precision of 1 μm, allowing the parallelism to be controlled to within one hundredth of a wavelength across the diameter of the sample at the frequencies typically used in our measurements; thus, interference effects due to non-parallelism of the

transducers were not a problem. Three clamping springs were used to apply sufficient bonding pressure to maintain good acoustic transmission. The sample holder also allowed the effects of sample strain on the ultrasonic velocity to be investigated. The strain ($\Delta L/L$, where L is the sample thickness) could be determined directly in most cases from the settings of the micrometer posts since the unstrained thickness was known accurately. Owing to the compressional rigidity of many of the samples studied, a large applied stress was necessary to achieve a measurable strain, leading to the undesirable possibility of warping the sample holder slightly and thus overestimating the strain. To ensure that accurate measurements of the strain were made, a capacitive technique was employed to measure ΔL directly. An annular capacitor, in guard-ring configuration, was affixed directly to the delay rods and carefully calibrated against the micrometer settings when no sample was present. This allowed the relative separation (and thus relative strain) to be determined within 0.2%. Absolute strains were determined to within 1%.

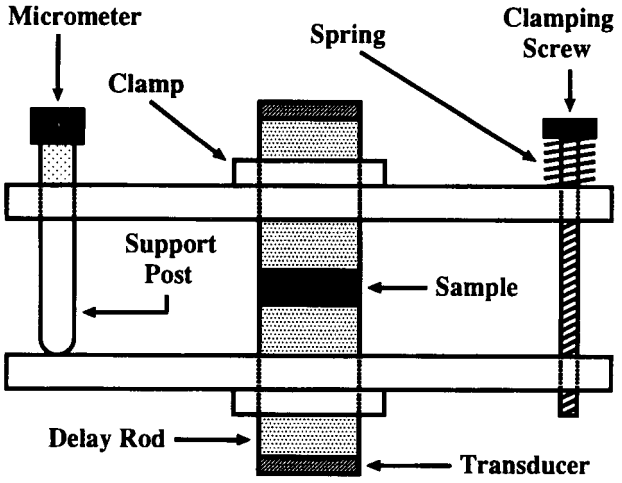

Figure 3. Sample holder, designed to allow precision ultrasonic transmission measurements to be performed without crushing the delicate sintered samples.

The faces of the disc-shaped transducers were coated with gold films to which electrical contacts were made. For a plane wave incident on such a piezoelectric detector, optimum sensitivity is achieved if the electrodes cover the entire surface of the transducer, since the detected voltage is the sum of the voltages generated at each point on the surface and these voltages add up in phase. This conventional piezoelectric transducer configuration was exploited for all the measurements of the weak ultrasonic signals that were transmitted ballistically (without scattering) through the samples. Reliable measurements were obtained in this way because the samples were sufficiently homogeneous at large length scales ($\gg \lambda$) that wavefront distortion of the ballistic signal, due, for example, to macroscopic variations in transit time in different regions of the sample, was negligible. Thus, there was no complication in these measurements arising from spurious cancellation of the ballistic signal in the detecting transducer, a problem which required the use of a new phase-insensitive transducer in some earlier measurements on very inhomogeneous samples [31]. In contrast, the large-area electrode configuration used for the ballistic measurements is totally unsuitable for measurements using piezoelectric transducers to detect the scattered ultrasonic signals that reach the detector after the ballistic pulse. Under the conditions of strong multiple

scattering that were encountered at high frequencies, the scattered signals undergo rapid spatial fluctuations of both amplitude and phase in the detecting plane and therefore average to almost zero if the net voltage across the transducer is measured. To make preliminary measurements of these multiply scattered signals, the gold film on one face of the transducer was replaced with a tiny electrode having a diameter of only 240 μm, with the remaining surface area of the transducer being covered by a grounding plane to avoid electrical pickup from nearby regions of the transducer. The diameter of this miniature electrode was much smaller than the ultrasonic wavelength in the delay rod for frequencies up to 20 MHz, thus ensuring that the signal was measured in a single coherence area, or speckle spot. By moving the miniature electrode across the surface of the transducer, the variation in the amplitude and phase of the scattered signals could be investigated.

The ultrasonic transmission time through the sample was determined precisely by measuring the delay between the central oscillations of the transmitted and reflected pulses. Measurements were also performed for time intervals one or more periods greater or less than the interval between the pulse centres. Errors due to phase shifts at the sample/delay-rod interfaces were eliminated by performing the measurements at several frequencies and extrapolating the delay data to their common value at zero period. A representative set of delay data is shown in figure 4, where it is seen that the measured changes in delay with frequency vary linearly with the period, implying that the phase shifts are independent of frequency, as expected. This procedure also allowed unambiguous determination of the central oscillations of the reflected and transmitted waveforms, thus eliminating a large potential source of error when measurements are made at a single frequency using a broad pulse containing many oscillations.

The ultrasonic attenuation in each sample was determined from the difference in

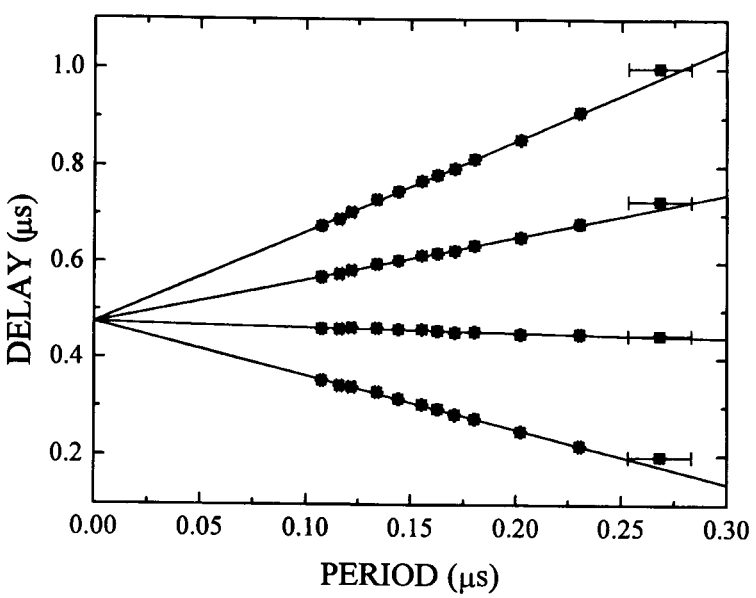

Figure 4. Delay time as a function of period. The true transit time, corrected for phase shifts at the sample interfaces, is obtained from the extrapolation to zero period, where the three lines meet.

amplitude between the pulse transmitted through the sample and a reference pulse generated by the reflection of the incident pulse at the first delay-rod/sample interface. For consistency, these measurements were also checked by comparing the relative amplitudes of the pulse transmitted through the sample/delay-rod 'sandwich' and the pulse transmitted through the delay rods only (when they were bonded together without the sample in place). Both sets of data were corrected for reflections at the interfaces owing to the difference in acoustic impedance between the sample and the quartz delay rods; this was straightforward since the calculation of the reflection and transmission coefficients depends on only the measured values of the densities and velocities for both materials. Some samples were smaller in surface area than the delay rods, necessitating a further correction for this area mismatch. Finally, estimates were also made of the transmission losses through the Nonaq bonding layers, although these were generally negligibly small compared with the very large attenuations that were measured in these experiments. After this preliminary analysis of the raw data, the two different methods of measuring the sample attenuation were found to be in excellent agreement, allowing the attenuation coefficient $\alpha(\omega)$, as defined by (5), to be determined.

4. Results and discussion

4.1. Structure and density

The sintered glass-bead samples used in our experiments were prepared over a wide range of occupied volume fractions ϕ, spanning values 0.18–0.50 for set A, and 0.25–0.64 for set B. By monitoring the structural integrity of a range of samples with low occupied volume fractions, we were able to establish the percolation threshold ϕ_c for our glass-bead network. This we found to be $\phi_c = 0.19 \pm 0.01$ from the observation that a sample with $\phi = 0.18$ disintegrated (i.e. no 'infinite' cluster) when the nickel was removed, while another sample with $\phi = 0.195$ remained (mostly) intact. This is somewhat larger than the value of $\phi_c = 0.15$ predicted for continuum percolation [32], the difference probably arising mainly from the polydispersity of the glass and nickel particles.

The structure of our sintered samples was investigated by analysing scanning electron micrographs of specially prepared two-dimensional cross sections of some of the samples. This circumvented the difficulties associated with attempts to obtain quantitative information on the positions of the particles by inspecting three-dimensional photographs such those shown in figure 1. To prepare the two-dimensional cross sections, the pores of the sinter were first filled with Stycast 1266 clear epoxy using a vacuum-impregnation technique, and a flat surface was then obtained by polishing the composite epoxy–sinter sample to a 1 μm finish. This epoxy, when freshly mixed, had a sufficiently low viscosity to penetrate the pores of the sinter and, when set, was sufficiently hard to prevent any beads from being removed during the polishing and to allow a flat surface to be readily obtained. The polished surfaces were coated with a thin carbon film to prevent charging by the electron beam of the SEM, and clear high-contrast micrographs of the glass/epoxy surfaces were obtained. The photographs were then digitized using a high-resolution scanner. Typical digitized micrographs for two of the sinters are shown in figure 5(*a*, *b*), where the light regions indicate the positions of the glass particles and the dark regions indicate the epoxy-filled voids.

For the sample shown in figure 5(*a*), the volume fraction occupied by the glass beads, as determined from the initial concentration of glass, was $\phi = 0.195$. Interestingly, the fraction of the total surface area of this micrograph that is filled with glass (i.e. the fraction

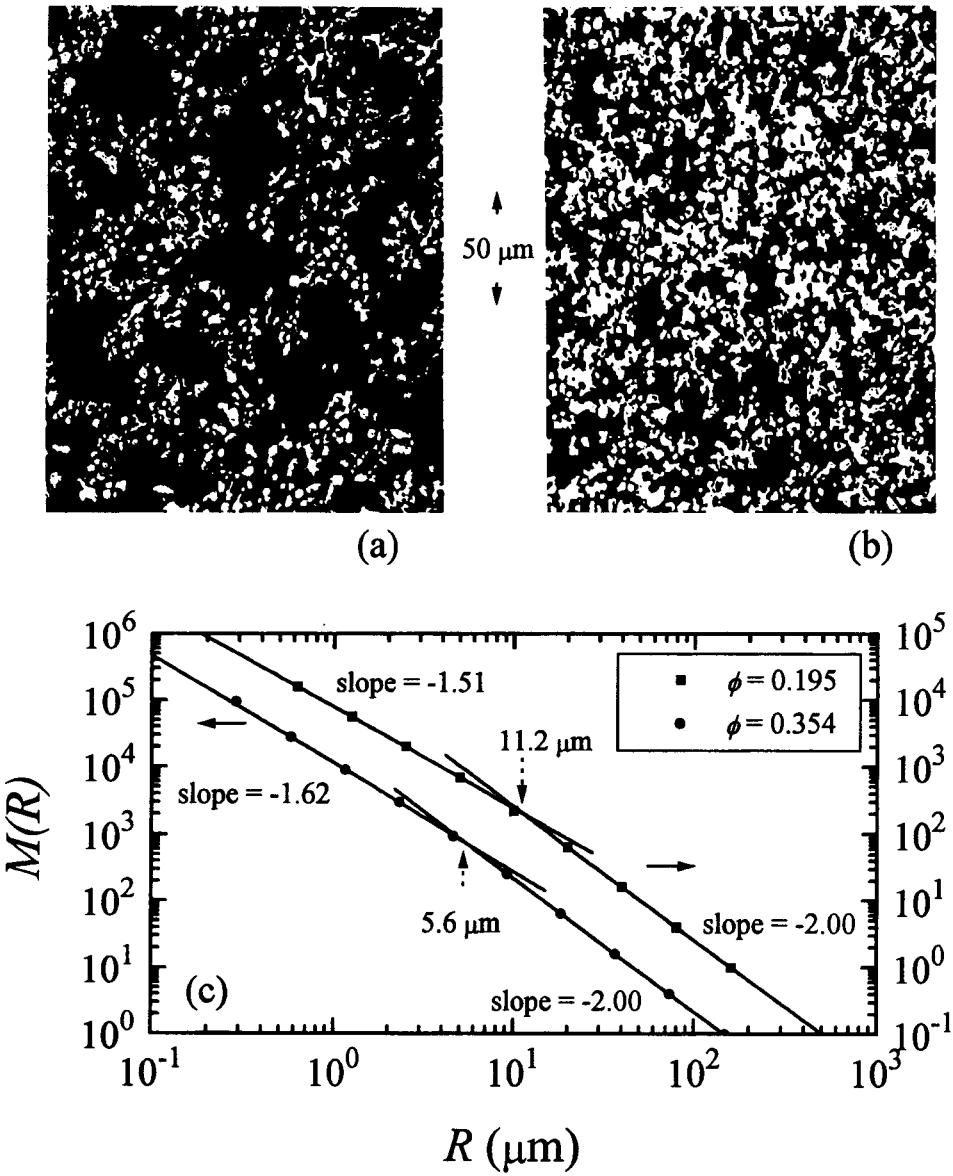

Figure 5. Top: Digitized micrographs of two-dimensional slices across sintered samples with occupied volume fractions, ϕ, of 0.195 (*a*) and 0.354 (*b*). The light areas represent the glass beads and the dark areas are the epoxy-filled voids. Bottom: The results of an analysis of the micrographs using a box counting algorithm to obtain estimates of the fractal dimension D and upper bounds for the percolation correlation length ξ for the two samples.

of the total area that is white) is equal to 0.191, which is extremely close to the value of ϕ determined from the initial glass concentration. Similar results were also found for the sample shown in figure 5(*b*), where the initial concentration of glass beads gave $\phi = 0.354$ and the glass surface-area fraction obtained from the micrograph is 0.356. These pictures,

therefore, must imply that very few, if any, of the beads are removed from the sample during the etching process, so that the beads belonging to small, isolated clusters remain trapped in the sample by the tenuous arms of the infinite percolating cluster. Of course, well above the percolation threshold, it is expected that the number of loose beads on finite clusters will be relatively few in number, although this is presumably not the case for the sample shown in figure 5(*a*). In any case, it is important to realize that these loose beads, which are not attached to the infinite cluster, have virtually no effect on the elastic and vibrational properties reported in this paper, since these properties are entirely dominated by the beads which are bonded to the infinite cluster that transmits the propagating ultrasonic waves.

The digitized photographs shown in figure 5 were analysed using a box counting technique [33, 34] that is a well established method for determining the fractal dimension D of images. The box counting algorithm divides the image into boxes of length R, and the number of boxes containing at least one white pixel, $M(R)$, is counted; when the image is a two-dimensional cross section of a fractal object embedded in a three-dimensional space, $M(R)$ is proportional to $R^{-(D-1)}$. The results of this analysis are summarized in the lower part of figure 5, which shows a log–log plot of $M(R)$ as a function of R for the two samples illustrated in figure 5(*a, b*). At short length scales, the slopes of the two curves are less than two, indicative of fractal correlations in the sinters. A least-squares fit to the data for the two samples gives estimates for D of 2.51 ± 0.05 and 2.6 ± 0.1, which are in agreement with the value of 2.5 expected for percolation in three dimensions. At larger length scales, there is a crossover to uniform Euclidean behaviour, as seen by the change in the slope to a value of -2, corresponding to a dimension $D = d = 3$. The length scales at which this crossover occurs are indicated on the figure; they give only a *lower* bound for the percolation correlation lengths ξ of each sample because of the likelihood that some beads from isolated, finite clusters are also present in the pictures, thereby reducing the size of the holes in the structure. Nonetheless, it is clear from these data that the correlation lengths are considerably larger than the bead radius a for the range of occupied volume fractions investigated, even though some of the samples were prepared with volume concentrations quite far from the percolation threshold. To confirm our analysis of the sinter structure, an independent determination of the fractal dimension and the crossover length was obtained by using an optical technique to measure the area autocorrelation function of a two-dimensional cross section of one of the samples [35], giving results which are in excellent agreement with the box counting method used above.

The sample density ρ, which was determined from measurements of the mass and volume after etching, was found to be less than the value determined from the initial density and occupied volume fraction of the glass beads. Data for both sample sets are shown in figure 6, where the ratio of the sinter density to the initial density of the individual glass beads, ρ/ρ_g, is plotted as a function of the occupied volume fraction ϕ. The solid line in the figure shows that the density ratio ρ/ρ_g is well parametrized by a linear dependence on ϕ of the form $\rho/\rho_g = 0.90\phi$. Remarkably, as indicated by the dashed curve, it is also possible to describe the data equally well for $\phi < 0.5$ by a power law of the form $\rho \propto (\phi - \phi_c)^{0.44}$, which is the behaviour predicted for the infinite cluster in percolation. However, this alternate interpretation of these data cannot be correct, because, as shown by the SEM micrographs in figure 5, not all the isolated glass clusters were washed out during the etching process, so that the measured density includes contributions from both the infinite cluster and isolated, finite clusters. Thus, the $\sim$10% reduction in the sample density indicated in figure 6 must result mainly from a reduction in the density of the individual glass beads themselves. The beads were made from a soda-lime glass, consisting typically of 73% SiO_2, 14% Na_2O and 10% CaO with trace amounts of metallic elements. For such a glass, the application of heat

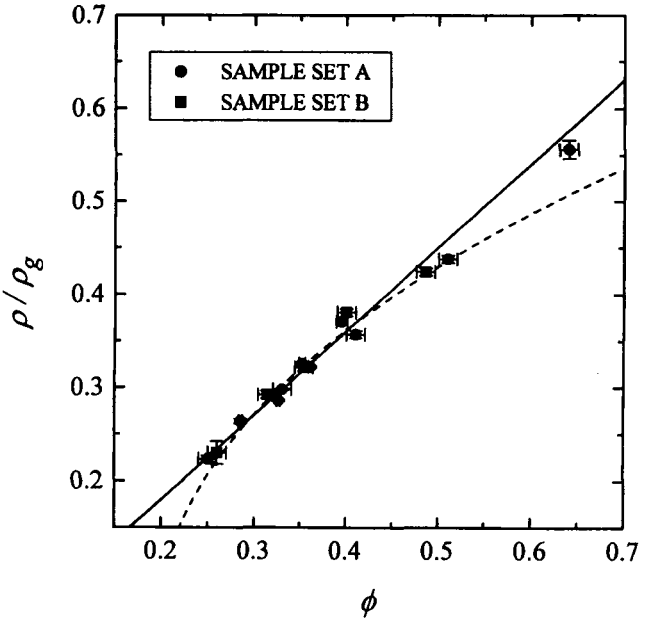

Figure 6. Dependence of the sinter density ρ, normalized by the density of the individual glass beads ρ_g, on occupied volume fraction ϕ. The solid line shows the best linear fit to the data, while the dashed line shows the results of fitting the data with a power law in $(\phi - \phi_c)$.

during sintering and the exposure to nitric acid during the extraction of the nickel particles are likely to conspire to cause significant leaching of the ionic impurities from this silicate glass, the effect being especially large for the Na_2O impurities [36]. Confirmation that this mechanism could be responsible for the density reduction was obtained by measuring the change in the Na/Si concentration ratio during sinter preparation using an energy dispersive analysis of x-rays (EDAX) spectrometer; although the non-ideal surface geometry of the samples studied allowed only a semi-quantitative analysis using this technique, the results indicated significant Na loss during the preparation procedure [35], giving results consistent with this explanation. Finally, we note that since the measured sample density for our system does not correspond to the density of the infinite cluster of the glass-bead percolation network, the density cannot be used as a scaling parameter in place of $\phi - \phi_c$ when comparing percolation theory with our measurements of the elastic and vibrational properties of the consolidated beads on the infinite cluster, as has been done for some other fractal systems [7].

4.2. Ultrasonic velocity

The ultrasonic velocity measures the rigidity of the network of consolidated glass beads, and hence, unlike the density, depends critically upon the microscopic character and strength of the bonds between beads. Thus, to make a meaningful comparison of experimental data with the theoretical predictions discussed in section 2, it is crucial to ensure that all samples in a given set are prepared under identical conditions. In practice, this requires meticulous control over the sintering time and temperature, as well as over the more subtle effects of packing, particle lubrication and pellet compression prior to sintering. These effects were all carefully controlled in taking the data presented in figure 7, which shows the dependence of

the ultrasonic velocity on the occupied volume fraction for the two sample sets investigated. In figure 7(*a*), we contrast the behaviour of the longitudinal and transverse velocities for sample set A, and show that the velocities for both polarizations scale with the occupied volume fraction as a power law with the same exponent, $y = 1.24$. Figure 7(*b*) compares the longitudinal velocities for the two sample sets; again the same scaling behaviour is found for set B as for set A, provided the occupied volume fraction does not exceed $\phi \approx 0.55$. However, there is a substantial difference in the magnitudes of the longitudinal velocities for the two sample sets. In set A, the large internal strains that were induced in the samples by the expansion of the nickel particles during oxidation resulted in bonds between the glass beads which were much weaker than those in samples from set B, and, as a consequence, a corresponding reduction in longitudinal velocity of approximately 30% was found. Despite this large difference in the magnitudes of the velocities, it is interesting to note that the *same* exponent describes the scaling of the velocities for the two sample sets, indicating that the presence of large internal strains in sample set A has not modified the nature of the microscopic elastic forces between the beads. These results therefore do not appear to support the idea, suggested by Alexander [37], that large internal strains cause scalar elasticity rather than vector elasticity to become dominant.

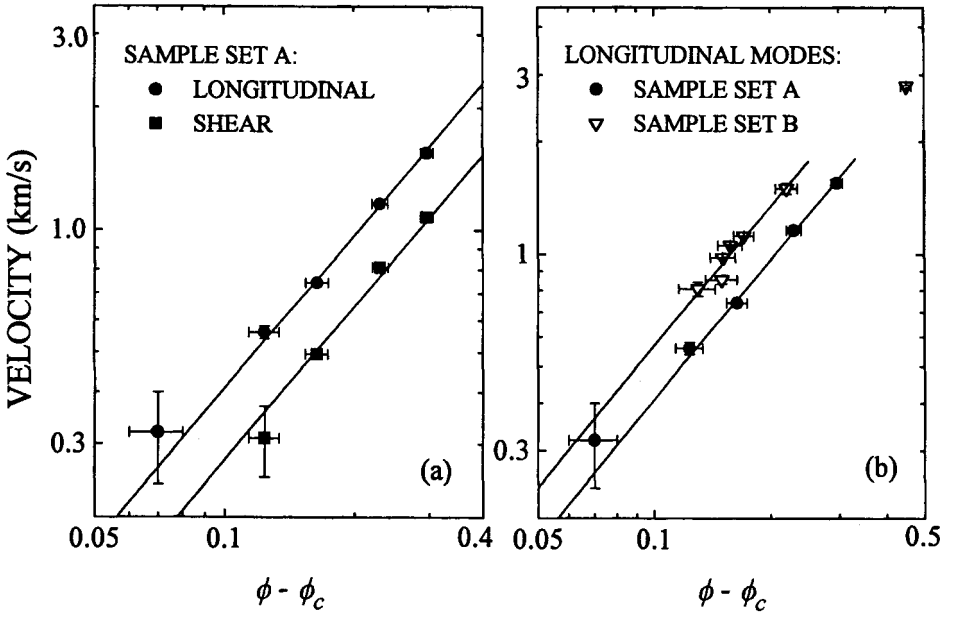

Figure 7. Dependence of the ultrasonic velocity on the distance from the percolation threshold, $\phi - \phi_c$. (*a*) compares the longitudinal and shear velocities for sample set A, while (*b*) compares the longitudinal velocities for the two sample sets.

The magnitude of the velocity exponent measured in our glass-bead samples, $y = 1.24 \pm 0.05$, is quite interesting, since it lies in between the values expected for the scalar and bond-bending elasticity models. This can be seen more clearly by calculating the corresponding values of the elasticity exponent and the fracton dimension for our samples. Since, from (2) and (3), $\tau = 2y + \beta$, we find $\tau = 2.9 \pm 0.1$, where we have used the accepted value of the exponent $\beta = 0.44$ [18]. Our value of $\tau = 2.9$ should be

compared with the best theoretical estimates in three dimensions of 2.0 and 3.75 for scalar and bond-bending elasticity respectively, as outlined in section 2. Similarly, from (2) we find $\tilde{d} = D/(1+y/\nu) = 1.04 \pm 0.05$, which again lies about halfway between the theoretical values of 4/3 and 0.87 for these models. While a velocity or elasticity exponent that differs from the predictions of scalar elasticity is expected for our vector percolation system, it *is* surprising that our exponent is so different from that of the bond-bending model, which has been shown previously to give an excellent description of the static elasticity and ultrasonic velocity of sintered metal powders [1, 3]. In particular, we note that this discrepancy does not appear to arise from a difference in the range of occupied volume fractions studied for the two systems, since the data shown in figure 7 extend over a similar range of $\phi - \phi_c$ to that of Deptuck *et al*, and that, because our value of ϕ_c is considerably larger, this range for our glass-bead samples actually corresponds to smaller values of the reduced occupied volume fraction $(\phi - \phi_c)/\phi_c$. Furthermore, we note that the cluster of cluster structure [3] of the sintered metal powders is much more complicated than the simple percolation structure of the glass-bead network used in the present study, so that realistic theoretical models of elasticity percolation should, if anything, be more applicable to our glass-bead samples.

Since the bond-bending model is widely believed to be the most realistic model of elasticity percolation, the lack of agreement between this model and our experimental data is intriguing. Although the theoretical estimates given above are derived for lattice percolation, this is not believed to be the cause of the discrepancy; continuum percolation models [38] give even higher values of the elasticity exponent, because of the presence of very weak bonds that are probably eliminated from our samples during the sintering process. Even though the present results extend as close to the percolation threshold as previous experiments on systems where the bond-bending model appears to give a good description of the data, it is still possible that our data are sufficiently far from threshold that the elasticity is not dominated by the weak bond-bending forces of singly connected chains that are invoked in the scaling arguments, but have an important contribution from central forces between multiply connected points in the network. This could certainly lower the effective elasticity exponent seen in the present experiments, although it remains an interesting theoretical challenge to investigate this possibility†. The most likely cause of the discrepancy between theory and experiment is the effect of increased connectivity between the beads resulting from the 25% polydispersity of the beads that is not accounted for in the model. Physically, the effect of increased connectivity is to stiffen the glass-bead network, so that, as the occupied volume fraction is lowered, the elasticity is reduced more gradually towards zero, corresponding to a smaller elasticity exponent. This effect has been demonstrated quantitatively by Stoll and Courtens [10], who used a numerical simulation of the structure of aerogel samples to show how increasing the connectivity of the network lowers the elasticity exponent and raises the spectral dimension exponent. Their demonstration of this effect is consistent with our data, even though the mechanism for the increased connectivity is different in aerogels than it is in our sinter samples. Finally, we mention one other experimental observation of an elasticity exponent similar to our value; Ye *et al* have measured an elasticity exponent of $\sim$2.5 near the dynamic rigidity percolation threshold in inverted micelles [39], a system in which, however, the underlying physics is

† It would, of course, also be interesting to extend our ultrasonic experiments to lower-density samples in order to see if there is a crossover to different scaling behaviour closer to ϕ_c; however, such experiments cannot be performed on samples made from the same glass beads, because the attenuation becomes prohibitively large at ultrasonic frequencies as the porosity increases, so that resolution of this question requires either ultrasonic experiments on a new set of samples assembled from smaller beads, or static elasticity experiments on samples similar to those used in the present work.

presumably quite different.

Additional information on the elasticity of our glass-bead network can be obtained by calculating Poisson's ratio ν_p for those samples where both the longitudinal and transverse sound velocities were measured. Poisson's ratio is an important characteristic of any solid, since it measures the amount of transverse expansion that results from a uniaxial compression. In terms of the longitudinal and shear sound velocities, v_L and v_S, Poisson's ratio is given by

$$\nu_p = \frac{v_L^2 - 2v_S^2}{2(v_L^2 - v_S^2)}. \tag{6}$$

The data for our samples are shown in figure 8(*a*) and indicate that ν_p is substantially lower than the values for most three-dimensional solids, where ν_p usually lies between 0.25 and 0.5. For ϕ in the range 0.3–0.5, we find that ν_p is typically about one quarter of the value for bulk glass ($\nu_p = 0.28$), while our lowest value, $\nu_p \sim 0.026 \pm 0.024$, is only about 10% of the bulk value. This reduction in ν_p is a rather dramatic consequence of the softening of the elasticity of the percolation network as ϕ is lowered, and suggests that ν_p may extrapolate to ~ 0 at $\phi = \phi_c$. Indeed, although there is very large scatter in our data for the two sample sets, these results are consistent with a numerical simulation for a cubic percolation network by Sahimi and Arbabi [21], who find that ν_p decreases monotonically as ϕ is lowered and that ν_p becomes slightly negative just above ϕ_c. This prediction of a slightly negative Poisson's ratio is intriguing, as it implies that the network collapses under a uniaxial stress but that this behaviour is reversible when the stress is removed, since the velocities or moduli that determine ν_p are defined in the elastic limit. It would be very interesting to see if such behaviour can be observed for our glass-bead percolation system by making precise and careful measurements of the elasticity closer to ϕ_c.

Interesting information on the elasticity of percolation networks near ϕ_c can also be obtained from the ratio of bulk to shear moduli, K/μ [24, 27, 28, 40]. Curiosity about this quantity was initially sparked by the conjecture [40] that this ratio approaches the universal value $4/d$ for percolation in d dimensions near ϕ_c, independent of the magnitude of the microscopic elastic constants. Subsequently, numerical simulations on a honeycomb lattice found a much larger value, ~ 2.5, for this ratio, leading Arbabi and Sahimi [28] to suggest $K/\mu = 8/z$ as a generalization of this conjecture for a network with coordination number z. This suggestion is consistent with simulations on both the honeycomb and simple cubic lattices, and gives the same numerical value as the Bergman–Kantor conjecture in the latter case. To compare these ideas with our longitudinal and shear velocity measurements on the glass-bead sinters, we plot in figure 8(*b*) the ϕ-dependence of the ratio v_L/v_S, which is an equivalent way of expressing the essential physics since v_L/v_S is simply related to K/μ by

$$\frac{v_L}{v_S} = \sqrt{\frac{K}{\mu} + \frac{4}{3}}. \tag{7}$$

While v_L/v_S is 1.8 for the bulk glass, the porous samples have smaller values, ranging from approximately 1.4 to 1.5. These values for the percolation system fall below the Bergman–Kantor conjecture, which gives $v_L/v_S = \sqrt{8/3} = 1.63$, but are very close to the behaviour expected from the Arbabi–Sahimi suggestion for a three-dimensional close-packed network. For a lattice-based percolation model, the coordination number for close-packing (FCC or HCP) is 12, which gives $v_L/v_S = \sqrt{2} = 1.41$, in good agreement with the behaviour expected at ϕ_c by extrapolating our data. For random percolation, the effective coordination number should be somewhat lower, typically in the range 10–11 as is found for liquids near

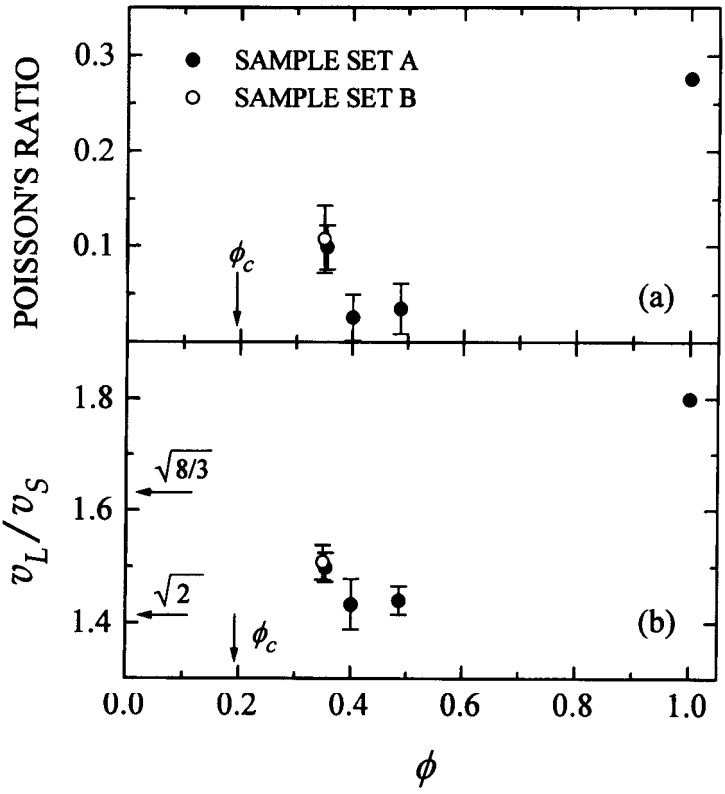

Figure 8. Dependence on occupied volume fraction of Poisson's ratio (*a*), and the ratio of longitudinal to shear velocities (*b*).

the freezing point, which only marginally raises the Arbabi–Sahimi prediction (to a value of $v_L/v_S = 1.46$ for $z = 10$) and is still in good agreement with our data. Thus, our results appear to rule out the original Bergman–Kantor conjecture, but they do support the idea that the ratio K/μ is given by $8/z$; this implies that K/μ is not universal, but depends on the type of network (although not on the details of the microscopic elastic interactions).

The data shown in figures 7 and 8 were obtained using low values of the sample strain ε; to investigate the effect on the velocity of increasing the strain, two additional samples were studied. The first sample had a density of $\rho = 690$ kg m^{-3} and an occupied volume fraction of 0.325 and allowed strains of up to 2% to be generated. Surprisingly, we found that the velocity decreases as the strain increases. This means that the sample becomes elastically weaker when compressively stressed, unlike most normal materials which become more rigid under compression. We find the rate at which the normalized velocity varies with the strain to be $v_0^{-1}\,\mathrm{d}v/\mathrm{d}\varepsilon = -0.03 \pm 0.02$, where v_0 is the velocity at zero strain and the strain is expressed as a percentage. This reduction in the velocity with increasing stress is also characteristic of fused quartz and many tetrahedrally coordinated glasses, and has been attributed to the existence of a double minimum in the angular dependence of the interatomic potential. The rate at which the normalized velocity varies with strain in the glass-bead sinters is comparable to that of fused quartz (−0.036) [41] and Pyrex glass (−0.05) [42]. This suggests that the nonlinear elasticity that gives rise to this effect in our porous glass-

bead sinters has its origin in the intrinsic nonlinear elastic properties of the glass beads themselves and not in the porous structure of the sinters. A similar result has been found in some silica aerogels having densities between 180 kg m^{-3} and 360 kg m^{-3} [43].

The second sample studied had a density of $\rho = 540$ kg m^{-3} and an occupied volume fraction of 0.247, which are somewhat lower than the corresponding values for the first sample; as a result the elasticity was even weaker, allowing strains of up to 4.5% to be generated. This sample was unlike the other samples on which velocity data are reported, in that it was known to exhibit very large scale ($\sim$1 mm) density fluctuations and had a significant number of microcracks. It was found, in contrast to the previous sample, that the velocity initially rose with increasing strain at a rate, $v_0^{-1}\,dv/d\varepsilon$, of about 0.15 before levelling off at a strain $\varepsilon \approx 3.5\%$, and then subsequently decreasing. This behaviour may be attributed to the effect of microcracks and density variations within the sample. With increasing strain, these microcracks, which serve to elastically weaken the sample, are forced to close, resulting in an increased velocity. The density fluctuations also imply that regions of the sample are elastically weaker with the result that they are more easily compressed. Consequently, it is not until the sample as a whole experiences a uniform stress distribution that the nonlinear scaling behaviour of the bulk glass begins to predominate and the velocity begins to decrease. This suggests that strain-dependent measurements of the velocity might serve as an appropriate method for diagnosing the presence of long-length-scale inhomogeneities and cracks in sample microstructure.

4.3. Ultrasonic attenuation

The ultrasonic attenuation was measured for each sample over as large a frequency range as possible, from a minimum frequency of 1 MHz up to a maximum frequency determined by the value at which the transmitted ballistic signal was about to become too small to be detectable. Typical data are shown in figure 9(*a*), where the longitudinal attenuation is plotted in dB cm^{-1} as a function of frequency for four samples from set A. For each sample, the attenuation increases very markedly with frequency, reaching extremely large values, up to $\sim$900 dB cm^{-1}, at the maximum attenuations that could be measured. These very large attenuations must result from elastic scattering from the voids in the porous glass network because ultrasonic absorption mechanisms are far too weak to explain the data: for example, absorption caused by internal friction in the glass beads themselves can cause attenuation of at most a few dB cm^{-1} in this frequency range [44]. Thus, these attenuation data are a direct measure of the frequency dependence of the scattering mean free path, given by $l_s(\omega) = 1/\alpha(\omega)$.

An important feature of the data, clearly seen in figure 9(*a*), is that the onset of strong attenuation occurs at lower frequencies, corresponding to longer wavelengths, in the more porous samples having lower values of the occupied volume fraction. This demonstrates very directly that the attenuation probes the distribution of pore sizes in the samples, and is especially sensitive to the largest pores, whose size grows as the porosity is increased. Note that the attenuation is determined by the scattering of waves propagating on the infinite cluster of consolidated beads; thus, it is not significantly influenced by any loose beads that remain in the sample after etching, since these are effectively decoupled acoustically from the infinite cluster, so that the pore size distribution probed by the attenuation corresponds to the voids in the infinite cluster. As a result, the attenuation can be meaningfully interpreted using the single-parameter scaling hypothesis introduced in the theory section, which states that the scattering behaviour should be the same in different samples as long as the ratio of the probing wavelength to the percolation correlation length remains constant. Thus, if

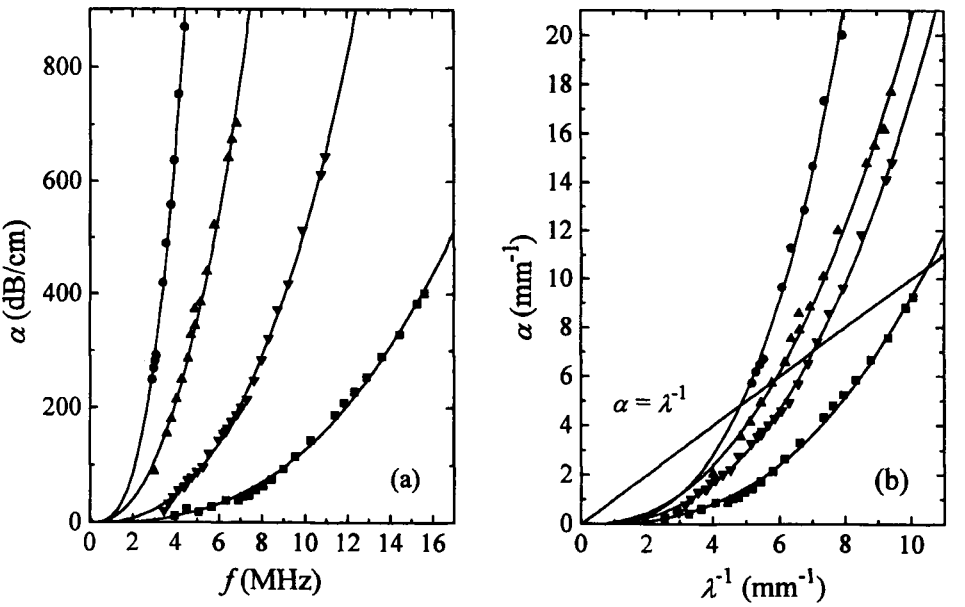

Figure 9. Longitudinal ultrasonic attenuation for four samples from set A, having occupied volume fractions of 0.314 (●), 0.354 (▲), 0.400 (▼) and 0.486 (■). The data are represented by the solid symbols, with the solid curves serving as guides to the eye, obtained by fitting a power law to the data. (*a*) The raw data as a function of frequency f. (*b*) The attenuation (in mm^{-1}) as a function of inverse wavelength (in mm^{-1}); the points at which the solid line $\alpha = \lambda^{-1}$ intersects the data give the characteristic scaling lengths l_c for each sample.

both the wavelength and the attenuation are scaled by this characteristic length, the data for different samples are expected to fall on a single common curve. Since independent measurements of the correlation length could not be reliably performed, as discussed in section 4.1, it was necessary to find an alternative characteristic length, which is proportional to the percolation correlation length, in order to investigate these scaling ideas. An empirical scaling length, that can be determined directly from the attenuation data, is the value of the scattering mean free path $l_s = \alpha^{-1}$ at an angular frequency ω such that the mean free path and the wavelength are equal [4]. At this frequency, the intensity of the ultrasonic wave drops to e^{-1} of its initial value as it propagates a single wavelength, a condition indicative of very strong scattering and the breakdown of coherent energy transport; it differs from the Ioffe–Regel criterion for localization, $kl_s = 1$, by a factor of 2π. This characteristic length l_c is defined by

$$l_c = l_s(\omega_c) = \lambda = 2\pi v/\omega_c. \tag{8}$$

It was determined from the data for each sample by converting the units of attenuation from dB cm^{-1} to mm^{-1} and plotting the attenuation as a function of the reciprocal of the wavelength, calculated by dividing the frequency by the measured sample velocity. This procedure is demonstrated in figure 9(*b*) for the longitudinal attenuation data for the set A samples. The points at which the straight line $\alpha = \lambda^{-1}$ intercepts the attenuation curves determine the proposed scaling lengths l_c for each sample.

Should single-parameter scaling arguments be valid, then multiplying the attenuation and the inverse wavelength by the corresponding values of l_c for each sample will collapse

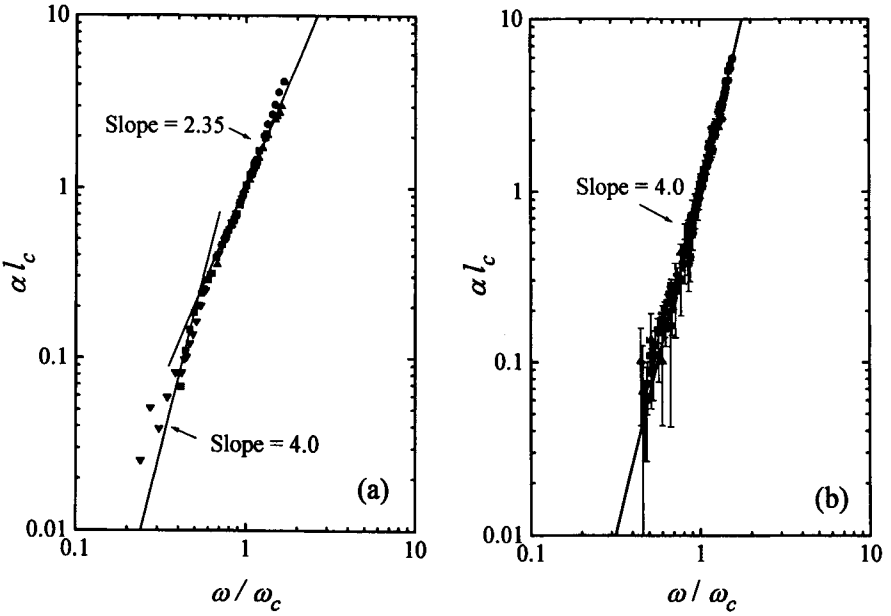

Figure 10. Frequency dependence of the scaled attenuation data for sample sets A (*a*) and B (*b*).

all the data to a common curve. This is exactly what is seen in figure 10, which shows a log–log plot of αl_c as a function of $\omega/\omega_c = l_c/\lambda$. In figure 10(*a*), the longitudinal and transverse scaled attenuation of samples from set A are shown, while in figure 10(*b*) the longitudinal scaled attenuations of samples from set B are plotted. The excellent scaling of the attenuation data shown in this figure clearly indicates that single-parameter scaling gives a correct description of our data, and also strongly supports our choice of l_c as a valid scaling length for the ultrasonic attenuation.

The frequency dependence of the scaled attenuation may be determined from the slopes of the lines in figure 10. Since Rayleigh scattering should dominate at low frequencies, where the wavelength is much larger than the sizes of the inhomogeneities, we expect the attenuation to vary as frequency to the fourth power. For set A (figure 10(*a*)), although it is plausible to draw a line of slope four through the data for the lower scaled frequencies, the data for the higher scaled frequencies are best described by a line of slope 2.35 ± 0.10. The most probable reason for this frequency dependence is the existence of sample inhomogeneities on length scales larger than the correlation length ξ, since a weaker than ω^4-dependence will occur if there are inhomogeneities with sizes of the order of the ultrasonic wavelength. A two-dimensional micrograph of one of the set A samples reveals the existence of density variations on length scales of order 100 μm, thereby confirming that the origin of the unexpected frequency dependence for these samples lies in non-uniformities at relatively large length scales, and not in more exotic mechanisms such as a possible crossover to weakly localized fractons [17, 35]. For set B (figure 10(*b*)), however, Rayleigh scattering is observed over the entire frequency range ($1.6 < kl_s < 60$) investigated (as expected for $k\xi > 1$), showing that the large-scale inhomogeneities responsible for the anomalous frequency dependence found in set A have been virtually eliminated in set B. This is, in fact, an important result since the improvements in sample preparation undertaken

for set B are essential for future experiments in which the frequency dependence of the mean free path is investigated at even shorter wavelengths, where $kl \sim 1$ and different behaviour associated with the crossover from phonons to fractons is predicted.

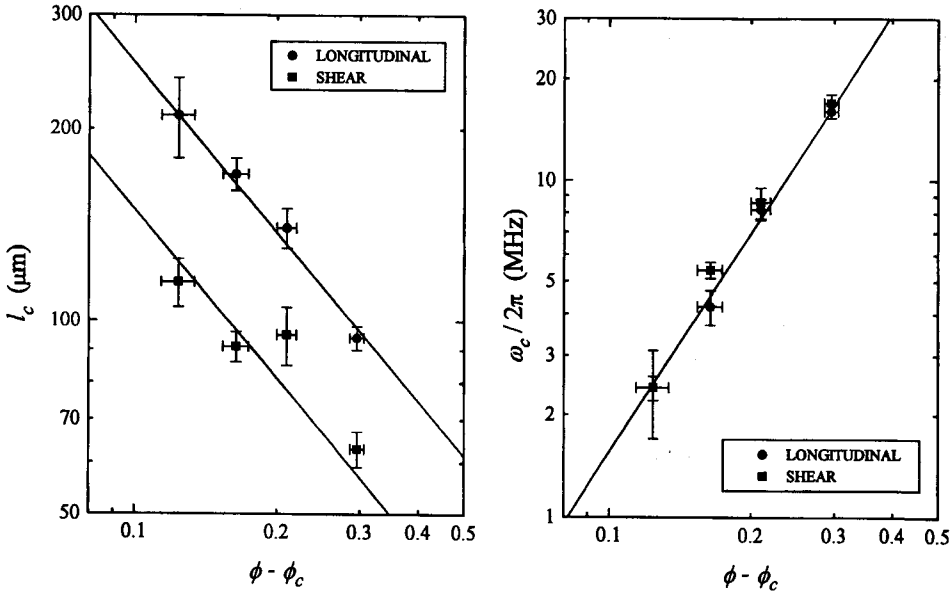

Figure 11. The characteristic scaling length l_c and frequency $\omega_c/2\pi$ plotted as a function of $\phi - \phi_c$ ((*a*) and (*b*), respectively).

A critical test of the applicability of percolation theory to the scaling of the attenuation data is whether or not l_c is proportional to the percolation correlation length ξ, i.e. whether or not $l_c \propto (\phi - \phi_c)^{-\nu}$ with $\nu = 0.88$. To investigate this question, we plot the values of l_c as a function of $\phi - \phi_c$ for sample set A in figure 11(*a*), where we have included the results for both longitudinal and shear modes. Although there is considerable scatter in the data, the variation of l_c with $\phi - \phi_c$ is certainly consistent with the behaviour expected from percolation theory, shown by the straight lines on this log–log plot that have been drawn with the predicted slope −0.88. However, these data also reveal a rather startling result, namely that the values of l_c differ for the longitudinal and shear polarizations. Since for each sample l_c is larger for longitudinal than for shear waves, this indicates that longitudinal waves undergo stronger scattering at the same wavelength (although the reverse holds when the scattering is compared at the same frequency). While this behaviour has not been anticipated for percolation structures, where theoretical treatments of the vibrational excitations have generally ignored the shear modes, a similar effect can be seen in data and theoretical models for the attenuation due to grain-boundary scattering in polycrystalline materials [45], although the microscopic details of the scattering must be very different in this system. The important implication of this result in our percolation system is that it suggests that there is not a unique length scale in the structure that determines the crossover length to localized modes [17], since the Ioffe–Regel criterion will be satisfied for each polarization at different wave vectors and mean free paths, so that the simple identity $k_{IR}^{-1} = l_{IR} = \xi$ cannot hold. Remarkably, however, our data indicate that there may be a unique scaling *frequency* for both polarization modes, as can be seen from figure 11(*b*) where the scaling frequency

$\omega_c = 2\pi v/l_c$ is plotted as a function of $\phi - \phi_c$. Thus, the difference in scattering strengths for the two polarizations compensates for the different propagation velocities of longitudinal and shear waves to give a single frequency and scattering time at which the crossover to localized modes will occur. Note also that the values we find for l_c also indicate that if it is correct to extrapolate our scattering data to somewhat higher frequencies in the phonon regime, the Ioffe–Regel criterion will be satisfied at values of the scattering mean free path that are well in excess of the bead radius, implying that there will be a range of wave vectors between k_{IR} and $1/a$ for which the strong localization of acoustic waves is likely to occur.

At frequencies above the maximum values at which the attenuation data in figures 9 and 10 were taken, the very strong scattering caused the ballistic component of the transmitted pulses to become immeasurably small for the sample thicknesses studied, the detection of the ballistic pulse being further complicated by the superposition of appreciable scattered signals. This scattered component of the transmitted acoustic field was investigated for one of the samples by replacing the conventional receiving transducers used for ballistic measurements by the point-electrode transducer that measures the transmitted signal over the very small area of only 0.05 mm^2. Since at the frequencies used this area is considerably less than λ^2, the signals were detected in a region over which the phase and amplitude of the detected sound field are expected to remain constant, thereby ensuring that there would not be any spurious reduction in the detected voltage due to phase cancellation across the active surface of the transducer. This allowed measurements of the scattered signals to be made in the strong multiple scattering regime, where, for the sample investigated using this technique, the scattering mean free paths were such that $kl_s < 2$ and $L/l_s > 10$. As a result of the strong scattering, the transmitted signal was spread out in time over a very extended interval ($\gg$ incident pulse width) after the initial arrival of the input pulse, as longer and longer multiple scattering paths made their way to the detector. The interference of these scattered waves caused a roughly periodic modulation of the transmitted signal, with an average period equal to the incident pulse width. This modulation time is equal to the coherence time of the signal, and corresponds to the range of path lengths that can simultaneously interfere in a pulsed experiment [44]. Fluctuations in the phase and amplitude of the scattered signals were also observed by varying the position of the detecting electrode on the surface of the receiving transducer, thus mapping out the speckle pattern of the scattered acoustic waves. The size of these large-amplitude fluctuations, whose standard deviation is of the same order of magnitude as the mean, was found to correspond roughly to the ultrasonic wavelength, as expected for the coherence area in the experimental situation where the detector is fairly close to the surface of the sample†.

Despite the success of these measurements in probing some of these basic interference effects of multiply scattered waves, further quantitative analysis of the multiply scattered data was precluded by limitations imposed by the delay-rod technique used in these experiments. Because the multiply scattered ultrasonic signals were so dispersed in time, reflections of the scattered waves both up and down the axis of the delay rods and off their side

† For these experiments the presence of the delay rod complicated the analysis of the speckle pattern, whose size was found to depend somewhat upon the time following the arrival of the input pulse that the spatial fluctuations were measured. When measured at a time within the first couple of microseconds of the scattered transmitted signal, the speckle width was about 4λ, the factor of 4 corresponding remarkably closely to the expected magnification factor of the speckle pattern for our delay-rod geometry, in which the distance between the detector and the sample was approximately four times the sample width. However, when analysed at later times, the speckle pattern became strongly influenced by scattering from the side walls of the delay rod, introducing additional interference effects that destroyed the usual magnification of the speckle pattern in the far field and causing the speckle size to shrink to the minimum possible value of $\sim\lambda^2$.

walls were superimposed on the signals emitted directly from the sample to the detector. These complications prevented the determination of the diffusion coefficient of the multiply scattered acoustic waves from the average time profile of the transmitted intensity, and thus also prevented an exploration of possible anomalous diffusion effects as the Ioffe–Regel condition was approached. In future work we plan to investigate these interesting possibilities using a different experimental approach that circumvents these constraints; in these experiments we shall take advantage of a method that we have used recently, in a different strongly scattering medium, to demonstrate the applicability of the diffusion approximation for multiply scattered sound [44].

5. Conclusions

A physical realization of a random structural percolation system has been constructed using sintered glass beads. The samples were prepared by controlling the positions of the voids in the glass-bead structure through the use of a temporary filler powder that was removed after sintering was complete; since the glass beads and the filler powder were of similar grain size and were thoroughly mixed before sintering the glass, the correspondence with a percolation structure was ensured. Ultrasonic experiments on these samples have allowed us to investigate the elasticity and vibrational dynamics of highly porous materials over a wide range of occupied volume fractions, and to compare these measurements with a number of interesting predictions of percolation theory.

Measurements of the ultrasonic velocity as a function of occupied volume fraction have shown that the elasticity exponent τ is equal to 2.9 ± 0.1 for this porous glass-bead network, and that the corresponding value of the fracton dimension $\tilde{d}$ is 1.04 ± 0.05. These values differ significantly from the values predicted by the bond-bending elasticity model, which is widely accepted as the most realistic model for describing the weakening of the elasticity of a percolating network as the occupied volume fraction of solid material is reduced. The most probable reason for this discrepancy is the increased connectivity of our glass-bead network arising from the 25% polydispersity of the beads themselves, which allows smaller beads to fill in bonds that would otherwise be left disconnected in a perfectly monodisperse system. This has the effect of stiffening the network, and causes a more gradual reduction in the elasticity as the occupied volume fraction is lowered, as reflected in the smaller elasticity exponent observed in our experiments. For some of our samples, our ultrasonic velocity measurements encompassed both longitudinal and shear modes, allowing us to investigate some general properties of elastic networks that are independent of the microscopic details of the elasticity. These experiments showed that both Poisson's ratio, ν_p, and the compressional to shear velocity ratio, v_L/v_S, are significantly reduced as the percolation threshold is approached. Relative to pure glass, Poisson's ratio is reduced by as much as an order of magnitude at the occupied volume fractions studied, suggesting that ν_p may vanish at threshold; in contrast, the ratio v_L/v_S decreases less dramatically, reaching values consistent with the Arbabi–Sahimi suggestion that the ratio of the bulk to shear moduli approaches the value $8/z$ at threshold, where z is the coordination number of the network. Measurements were also performed to look directly at the strain dependence of the velocity, showing that such measurements can probe the microscopic nonlinear elastic properties of the glass beads, as well as the presence of macroscopic inhomogeneities and cracks that can be problematic in the manufacture of porous materials.

The attenuation of the ballistic component of the ultrasonic signals was measured to determine the frequency dependence of the scattering mean free path in these strongly scattering samples. Over the range of frequencies for which this ballistic pulse could

be detected, the scattering mean free path was found to decrease dramatically, reaching values as low as $l_s \sim 1.6/k$ in these experiments, indicative of the very strong scattering encountered as the wavelength was reduced. By studying the variation of the attenuation with occupied volume fraction, it was clearly demonstrated that the attenuation is strongly dependent on the range of pore sizes in the samples. This behaviour was investigated by scaling the attenuation data for different samples using a characteristic length l_c determined by the strong scattering condition that the mean free path and the wavelength be equal. This characteristic length was found to scale with occupied volume fraction in the same way as the percolation correlation length, as expected for single-parameter scaling in a percolation system. Interestingly, l_c was found to be different for longitudinal and shear waves, reflecting differences in the strength of the scattering for these two modes of propagation; however, the corresponding frequency $\omega_c = 2\pi v/l_c$ was found to be the same for both modes, suggesting that there may be a single crossover frequency, rather than wavelength or wave vector, that characterizes the breakdown of the coherent propagation of acoustic waves due to the very strong scattering.

In this paper, we have demonstrated that the sample preparation procedure developed for these experiments can successfully produce porous materials with interesting acoustic properties that can be meaningfully interpreted using percolation and fractal scaling ideas. Here, we have concentrated on the physics of ballistic propagation, which dominates the acoustic transport in the low-frequency phonon regime, and which undergoes progressively stronger and stronger scattering as the frequency is increased. In future work, we plan to extend these measurements to higher frequencies using a different experimental approach that will enable us to investigate the behaviour of the multiply scattered sound, and to look for possible anomalous diffusive effects associated with the predicted crossover from phonon to fracton behaviour.

Acknowledgments

This research has been supported by the Natural Sciences and Engineering Research Council of Canada. HPS wishes to acknowledge the support of a University of Manitoba Graduate Fellowship. We should also like to acknowledge the assistance of G Cosby for preparing some of the earlier samples, and K Beaty for analysing the scanning electron micrographs of the samples.

References

[1] Deptuck D, Harrison J D and Zawadzki P 1985 Measurement of elasticity and conductivity of a three-dimensional percolation system *Phys. Rev. Lett.* **54** 913–6

[2] Kantor Y and Webman I 1984 Elastic properties of random percolating systems *Phys. Rev. Lett.* **52** 1891–4

[3] Maliepaard M C, Page J H, Harrison J P and Stubbs R J 1985 Ultrasonic studies of the vibrational modes of sintered metal powders *Phys. Rev.* B **32** 6261–71

[4] Page J H and McCulloch R D 1986 Ultrasound propagation in sintered metal powder: evidence of a crossover from phonons to fractons *Phys. Rev. Lett.* **57** 1324–7

[5] Nakayama T, Yakubo K and Orbach R L 1994 Dynamical properties of fractal networks: scaling, numerical simulations, and physical realizations *Rev. Mod. Phys.* **66** 381–443

[6] Vacher R, Woignier T, Pelous J and Courtens E 1988 Structure and self-similarity of silica aerogels *Phys. Rev.* B **37** 6500–3

[7] Courtens E, Pelous J, Phalippou J, Vacher R and Woignier T 1987 Brillouin-scattering measurements of phonon–fracton crossover in silica aerogels *Phys. Rev. Lett.* **58** 128–31

[8] Courtens E, Vacher R, Pelous J and Woignier T 1988 Observation of fractons in silica aerogels *Europhys. Lett.* **6** 245–50

[9] Courtens E and Vacher R 1992 Structure and dynamics of silica aerogels *Phil. Mag.* B **65** 347–55
[10] Stoll E and Courtens E 1990 Connectivity and the fractal dimension of percolation clusters *Z. Phys.* B **81** 1–2
[11] Pachet N and Page J H 1989 Ultrasonic velocity and attenuation in a glass-bead percolation system *Phonons 89* ed S Hunklinger *et al* (Singapore: World Scientific) pp 679–81
[12] Schriemer H P and Page J H 1992 Ultrasonic investigation of acoustic phonons at megaHertz frequencies in sintered glass-bead networks *Phonon Scattering in Condensed Matter VII (Springer Series in Solid State Sciences)* ed M Meisser and R O Pohl (Berlin: Springer) pp 281–2
[13] Stauffer D 1985 *Introduction to Percolation Theory* (London: Taylor and Francis)
[14] Roux S and Guyon E 1986 Transport exponents in percolation *On Growth and Form* ed E Stanley and N Ostrowsky (Dordrecht: Nijhoff) pp 273–7
[15] Alexander A and Orbach R 1982 Density of states on fractals: 'fractons' *J. Physique* **43** 625–31
[16] Rammal R and Toulouse G 1983 Random walks on fractal structures and percolation clusters *J. Physique Lett.* **44** L13–22
[17] Aharony A, Alexander S, Entin-Wohlman O and Orbach R 1986 Scattering of fractons, the Ioffe–Regel criterion, and the 4/3 conjecture *Phys. Rev. Lett.* **58** 132–5
[18] Stauffer D 1986 Percolation and cluster size distribution *On Growth and Form* ed E Stanley and N Ostrowsky (Dordrecht: Nijhoff) pp 79–100
[19] Webman I and Grest G S 1984 Dynamic behaviour of fractal structures *Phys. Rev.* B **31** 1689–92
[20] Born M and Huang K 1954 *Dynamical Theory of Crystal Lattices* (New York: Oxford University Press)
[21] Sahimi M and Arbabi S 1993 Mechanics of disordered solids. II. Percolation on elastic networks with bond-bending forces *Phys. Rev.* B **47** 703–12
[22] Feng S, Sen P N, Halperin B I and Lobb C J 1984 Percolation on two-dimensional elastic networks with rotationally invariant bond-bending forces *Phys. Rev.* B **30** 5386–9
[23] Feng S and Sahimi M 1985 Position-space renormalization for elastic percolation networks with bond-bending forces *Phys. Rev.* B **31** 1671–3
[24] Bergman D J 1985 Elastic moduli near percolation: universal ratio and critical exponent *Phys. Rev.* B **31** 1696–8
[25] Roux S 1986 Relation between elastic and scalar transport exponent in percolation *J. Phys. A: Math. Gen.* **19** L351–6
[26] Sahimi M 1986 Relation between the critical exponent of elastic percolation networks and the conductivity and geometrical exponents *J. Phys. C: Solid State Phys.* **19** L79–83
[27] Zabolitsky J G, Bergman D J and Stauffer D 1986 Precision calculation of elasticity for percolation *J. Stat. Phys.* **44** 211–23
[28] Arbabi S and Sahimi M 1988 Elastic properties of three dimensional percolation networks with stretching and bond-bending forces *Phys. Rev.* B **38** 7173–6
[29] Ioffe A F and Regel A R 1960 *Prog. Semicond.* **4** 237
[30] Song Y, Noh T W, Lee S and Gaines J R 1986 Experimental study of the three-dimensional AC conductivity and dielectric constant of a conductor-insulator composite near the percolation threshold *Phys. Rev.* B **33** 904–8
[31] Page J H and McCulloch R D 1986 Phase-insensitive measurements of ultrasonic attenuation near the phonon–fracton crossover in sintered powder *Phonon Scattering in Condensed Matter V (Springer Series in Solid-State Sciences)* ed A C Anderson and J P Wolfe (Berlin: Springer) pp 221-3
[32] Cohen M H, Jortner J and Webman I 1977 *Electrical Transport and Optical Properties of Inhomogeneous Media* ed J C Garland and D B Tanner (New York: AIP)
[33] Liebovitch L S and Toth T 1989 A fast algorithm to determine fractal dimensions by box counting *Phys. Lett.* **141A** 386–90
[34] Huang Q, Lorch J R and Dubes R C 1994 Can the fractal dimension of images be measured? *Pattern Recog.* **27** 339–49
[35] Pachet N G 1990 Ultrasonic velocity and attenuation in a glass-bead percolation system *MSc Thesis* University of Manitoba, Winnipeg
[36] Paul A 1982 *Chemistry of Glasses* (London: Chapman and Hall)
[37] Alexander A 1984 Is the elastic energy of amorphous materials rotationally invariant? *J. Physique* **45** 1939–45
[38] Halperin B I, Feng S and Sen P N 1985 Differences between lattice and continuum percolation transport exponents *Phys. Rev. Lett.* **54** 2391–4
[39] Ye L, Weitz D A, Sheng P, Bhattacharya S, Huang J S and Higgins M J 1989 Dynamics rigidity percolation in inverted micelles *Phys. Rev. Lett.* **63** 263–6
[40] Bergman D J and Kantor Y 1984 Critical properties of an elastic fractal *Phys. Rev. Lett.* **53** 511–4

[41] Bogardus E H 1965 Third-order elastic constants of Ge, MgO, and fused SiO *J. Appl. Phys.* **36** 2504–13
[42] Hughes D S and Kelly J L 1953 Second-order elastic deformations of solids *Phys. Rev.* **92** 1145–9
[43] Xhonneux P, Courtens E, Pelous J and Vacher R 1989 Scaling nonlinear elasticity in silica aerogels *Europhys. Lett.* **10** 733–8
[44] Page J H, Schriemer H P, Bailey A E and Weitz D A 1995 Experimental test of the diffusion approximation for multiply scattered sound *Phys. Rev.* E **52** 3106–14
[45] Papadakis E P 1981 Scattering in polycrystalline media *Ultrasonics, Methods of Experimental Physics* **19** ed P D Edmonds (New York: Academic) pp 237–98